Chinese Chemical Letters 35 (2024) 109632

Contents lists available at ScienceDirect

Chinese Chemical Letters

journal homepage: www.elsevier.com/locate/cclet

Macrophages-mediated tumor accumulation and deep penetration of bismuth/manganese biomineralized nanoparticles for enhanced radiotherapy

Jiahao Liu[a,b,1], Peng Liu[c,d,1], Junhong Duan[b], Qiongxuan Xie[e], Jie Feng[a], Hongpei Tan[b], Ze Mi[b], Ying Li[f], Yunjie Liao[b], Pengfei Rong[b,*], Wenhu Zhou[a,*], Xiang Gao[g,*]

[a] Xiangya School of Pharmaceutical Sciences, Central South University, Changsha 410013, China
[b] Department of Radiology, The Third Xiangya Hospital, Central South University, Changsha 410013, China
[c] Department of Nuclear Medicine, XiangYa Hospital, Central South University, Changsha 410008, China
[d] Key Laboratory of Biological Nanotechnology, NHC, Changsha 410013, China
[e] Department of Oncology, Xiangya Hospital, Central South University, Changsha 410008, China
[f] Department of Nursing, Hunan Provincial People's Hospital (The First Affiliated Hospital of Hunan Normal University), Changsha 410005, China
[g] State Key Laboratory of Toxicology and Medical Countermeasures, Institute of Pharmacology and Toxicology, Beijing 100050, China

ARTICLE INFO

Article history:
Received 10 November 2023
Revised 6 February 2024
Accepted 7 February 2024
Available online 10 February 2024

Keywords:
Radiotherapy sensitizers
Metal-based nanoparticles
Targeted nanoparticle delivery
STING pathway activation
Sequential radiotherapy

ABSTRACT

Radiotherapy (RT) is a widely used cancer treatment, and the use of metal-based nano-radiotherapy sensitizers has shown promise in enhancing its efficacy. However, efficient accumulation and deep penetration of these sensitizers within tumors remain challenging. In this study, we present the development of bismuth/manganese biomineralized nanoparticles (BiMn/BSA) with multiple radiosensitizing mechanisms, including high atomic number element-mediated radiation capture, catalase-mimic oxygenation, and activation of the stimulator of interferon genes (STING) pathway. Significantly, we demonstrate that low-dose RT induces the recruitment of macrophages and subsequent upregulation of Matrix metalloproteinases (MMP)-2 and MMP-9 that degrade the extracellular matrix (ECM). This dynamic process facilitates the targeted delivery and deep penetration of BiMn/BSA nanoparticles within tumors, thereby enhancing the effectiveness of RT. By combining low-dose RT with BiMn/BSA nanoparticles, we achieved complete suppression of tumor growth in mice with excellent biocompatibility. This study provides a novel and clinically relevant strategy for targeted nanoparticle delivery to tumors, and establishes a safe and effective sequential radiotherapy approach for cancer treatment. These findings hold great promise for improving the outcomes of RT and advancing the field of nanomedicine in cancer therapy.

Radiotherapy (RT) is a commonly used treatment for cancer [1], but its clinical application is limited by several factors [2,3]. One major challenge is the difficulty in delivering high doses of radiation to tumors while minimizing damage to surrounding healthy tissue [4–6]. This can lead to suboptimal treatment outcomes, as low doses may not be effective in killing cancer cells while high doses can cause serious side effects. Another limitation is the development of radiotherapy resistance in tumors, particularly in solid tumors that are often hypoxic. This resistance can occur through various mechanisms, including DNA repair, cell cycle regulation, and changes in the tumor microenvironment [2,7-9]. As a result, there is a need to develop new strategies to enhance the effectiveness of radiotherapy and overcome these clinical challenges.

In recent years, metal-based nano-radiotherapy sensitizers have gained attention from researchers due to their potential to enhance radiotherapy through various mechanisms [10–12]. Firstly, high-*Z* elements-based nanomaterials, like tungsten, platinum, gold, and bismuth, can increase the capture cross-section of X-ray photons and Compton scattering effect, generating additional secondary electrons that can augment the cellular exposure to ionizing radiation-induced reactive oxygen species (ROS) and DNA damage [13–15]. Secondly, various metal-based nanoparticles have been developed that have intrinsic catalytic activity to produce O_2 using tumor abundant H_2O_2 as a substrate for hypoxia alleviation [16,17]. Thirdly, recent studies have shown that Mn-based nanoparticles can activate the stimulator of interferon genes (STING) signaling pathway by releasing Mn^{2+}, thereby enhancing the effect

* Corresponding authors.
E-mail addresses: rongpengfei66@163.com (P. Rong), zhouwenhuyaoji@163.com (W. Zhou), gaoxiang609@163.com (X. Gao).
[1] These authors contributed equally to this work.

https://doi.org/10.1016/j.cclet.2024.109632
1001-8417/

of radiotherapy [18–21]. Therefore, metal-based nano-radiotherapy sensitizers hold great promise for improving the efficacy of cancer radiotherapy. By combining multiple mechanisms and developing more targeted delivery methods, it may be possible to further enhance the effectiveness of these sensitizers and improve patient outcomes [22,23].

The effectiveness of nano-radiotherapy sensitizers is dependent on their ability to accumulate in tumor tissues and be uniformly distributed throughout the tumor area [24]. However, despite the use of tumor-targeting strategies such as the enhanced permeability and retention (EPR) effect, the overall efficiency of nanoparticle delivery to tumors remains suboptimal. Studies have shown that only an estimated 0.7% of administered nanotherapeutics successfully infiltrate solid tumors, with the majority accumulating around the tumor periphery [25]. This limited penetration is attributed to the unique pathophysiological features of tumors, including a densely packed extracellular matrix, elevated interstitial fluid pressure, and aberrantly structured tumor vasculature [26]. These factors collectively restrict the deep penetration and effective diffusion of nanoparticle drugs, resulting in inadequate reach to the hypoxic tumor core [27]. As a result, poor treatment outcomes and tumor recurrence can occur. Therefore, the development of innovative delivery strategies aimed at bolstering the accumulation and penetration of nano-radiotherapy sensitizers within tumors is crucial for enhancing radiotherapy efficacy.

Recently, our research group, along with others, has made an intriguing discovery regarding the recruitment of macrophages to local tumor microvessels through low-dose radiotherapy [28,29]. This phenomenon has been found to significantly enhance the tumor-targeting accumulation of nanoparticles by leveraging the vasculature bursting effect. We have observed that the recruitment of macrophages is a dynamic process, reaching its peak on the third day following radiotherapy. Exploiting this temporal window, we have successfully amplified the enrichment of nanoparticles at the tumor site by a remarkable 26-fold. Importantly, macrophages play a crucial role in regulating the tumor microenvironment and are capable of degrading tumor extracellular matrix (ECM) of tumor through the secretion of metalloproteinases (MMP-2 and MMP-9) [30]. Consequently, we hypothesize that the recruitment of macrophages induced by low-dose radiotherapy not only enhances the targeting of nanoparticles to tumors, but also facilitates their deeper penetration into the tumor microenvironment.

To support our hypothesis, we developed a biomineralization process using bovine serum albumin (BSA) as a template to create a multifunctional nanoradiosensitizer (Scheme 1). This nanoradiosensitizer, named BiMn/BSA, incorporates bismuth-manganese bimetallics and possesses multiple radiosensitizing mechanisms, including the high atomic number (Z) element of bismuth, catalytic oxygenation through its catalase-mimic activity, and activation of the STING pathway upon intracellular release of Mn^{2+}. Using this nanoradiosensitizer, we investigated the efficacy of low-dose radiotherapy in inducing macrophage recruitment and its impact on the tumor-targeting delivery and penetration of nanoparticles within the tumor. Our results demonstrate that low-dose radiotherapy effectively recruits macrophages, which in turn dynamically modulate the ECM by upregulating MMP-2 and MMP-9. The recruitment of macrophages and ECM degradation play crucial roles in enhancing the accumulation and intratumoral penetration of nanoparticles, respectively. Furthermore, by combining a second round of low-dose radiotherapy, we achieved complete suppression of tumor growth while ensuring full biocompatibility in tumor-bearing mice. This study introduces a novel strategy for targeted nanoparticle delivery to tumors and develops a safe and effective sequential radiotherapy approach for cancer treatment by combining low-dose radiotherapy with nanoradiosensitizers.

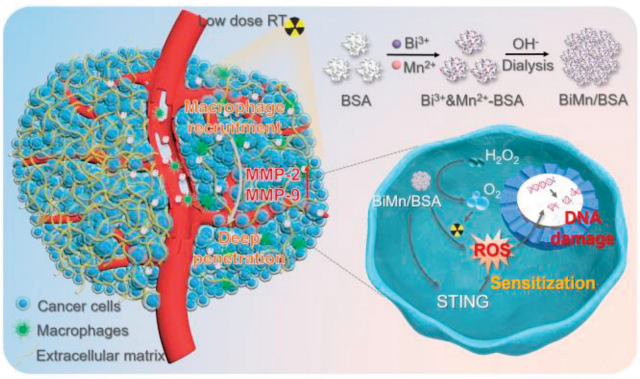

Scheme 1. Schematic illustration of the preparation BiMn/BSA, and mechanisms of low-dose radiation to promote the accumulation and intratumoral penetration of BiMn/BSA for effective sequential RT.

BiMn/BSA nanoparticles were synthesized through a facile biomineralization process, in which BSA served as template by virtue of its strong coordination with both Bi^{3+} and Mn^{2+} [31,32]. The biomineralization was triggered upon addition of NaOH to allow nucleation, crystal growth, and the formation of BiMn/BSA nanoparticles. Transmission electron microscope (TEM) images showed that BiMn/BSA had a uniform platelike structure with an average diameter of about 110 nm (Fig. 1A and Fig. S1 in Supporting information), consistent with the dynamic light scattering (DLS) measurement (Fig. 1B). The elemental mapping was performed to probe the structural components of BiMn/BSA, and C, O, N, S, Bi and Mn were noticed (Fig. 1C), confirming the BSA-mediated Bi/Mn biomineralization. X-ray photoelectron spectroscopy (XPS) was also applied to determine the composition of Bi and Mn in the BiMn/BSA. The characteristic binding energy peaks at 171.78 and 158.63 eV were assigned to Bi $4f_{5/2}$ and Bi $4f_{7/2}$, respectively, while the peaks at 658.23 and 641.88 eV were attributed to Mn ($2p_{1/2}$) and Mn ($2p_{3/2}$) (Figs. 1D–F). In addition, the content of Bi and Mn in BiMn/BSA was measured *via* inductively coupled plasma atomic emission spectroscopy (ICP-AES), which turned out to be 1.1% and 0.87% respectively (Fig. 1G).

To study the colloidal stability, BiMn/BSA was redispersed in phosphate buffered saline (PBS) or fetal bovine serum (FBS)-contained DMEM cell medium, and the hydrodynamic size was monitored. The size was almost unchanged over 48 h (Fig. 1H), demonstrating the stability of the nanoparticles for biological applications. With Mn element integration, the nanoparticles were designed to equip with catalase-mimic activity to relief tumor hypoxia and reinforce the efficacy of oxygen-dependent RT. To confirm this, H_2O_2 was added into BiMn/BSA, and the oxygenation was measured by using a portable dissolved oxygen meter. As expected, a rapid O_2 generation kinetic was observed in 10 min (Fig. 1I). Meanwhile, the Mn/BSA also exhibited excellent capability to produce oxygen by decomposing H_2O_2 (Fig. S2 in Supporting information). For nanoparticles without Mn (termed Bi/BSA), by contrast, no such phenomenon was seen. Therefore, the catalytic-oxygenation capability was derived from Mn component, which was consistent with previous reports [33–35]. Moreover, O_2 generation rate increased with higher BiMn/BSA concentrations, displaying a concentration-dependent profile (Fig. 1J).

The other biomineralized metal, Bi, which has the highest atomic number amongst non-radioactive metals ($Z = 83$), could significantly adsorb radiation energy to sensitize radiotherapy. To verify such function of Bi-containing nanoparticles, radiation was performed on mouse origin (4T1) tumor cell lines tumor and human origin tumor cell lines (MDA-MB-231), and anti-tumor effect was evaluated by cell counting kit-8 (CCK8) assay. Without radiation, both Mn/BSA, Bi/BSA and BiMn/BSA showed minimal cyto-

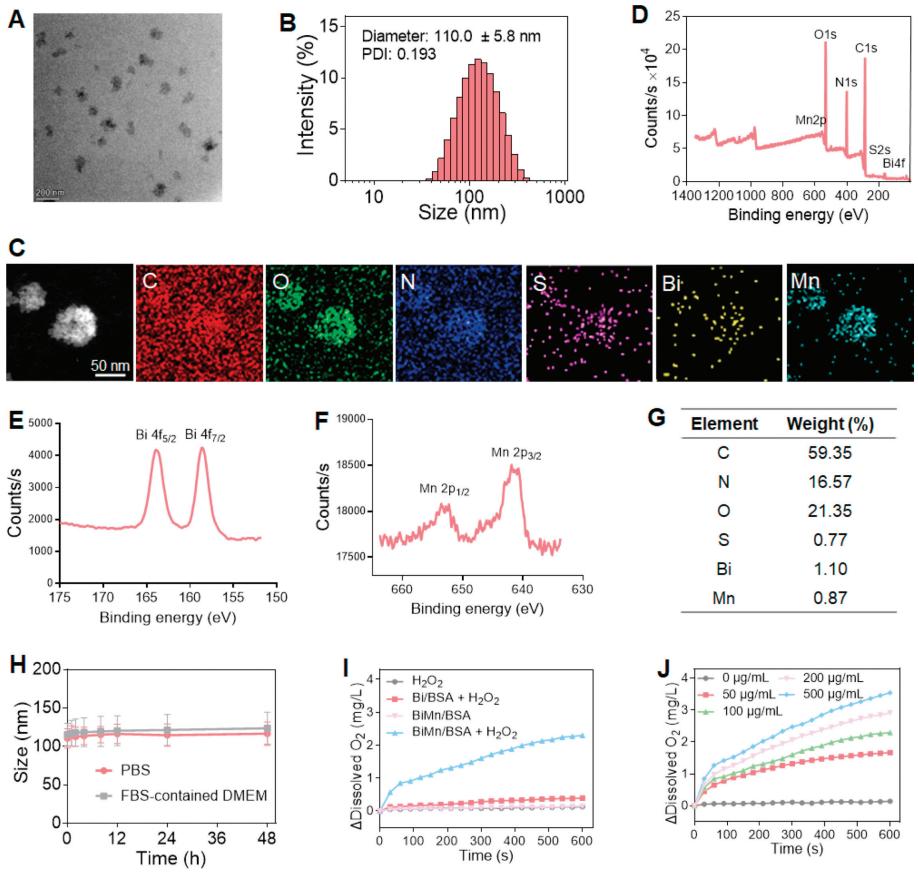

Fig. 1. (A) TEM image. Scale bar: 200 nm. (B) hydrodynamic size and (C) element mapping of BiMn/BSA. (D) XPS spectra showed the survey spectrum. (E) Bi 4f and (F) Mn 2p orbitals of BiMn/BSA. (G) The element content of BiMn/BSA was measured by ICP-OES. (H) Dynamic monitoring the particle size of BiMn/BSA in PBS and FBS-contained DMEM. Oxygen generation in H_2O_2 solutions after adding (I) various formulations and (J) different concentrations of BiMn/BSA. Quantitative results are presented as standard deviation (SD) ($n = 3$). Differences among multiple groups were assessed using one-way ANOVA.

toxicity (Figs. 2A and B, Fig. S3 in Supporting information), indicating biocompatibility of the nanoparticles. Upon exposure to radiation with 4 Gy dose, by contrast, Bi/BSA and BiMn/BSA could kill tumor cells in a concentration-dependent manner, demonstrating the sensitization effect. We then tested various radiation doses, and radio-sensitization was still observed (Figs. 2C and D). Interestingly, BiMn/BSA showed relatively stronger cell damage activity than Bi/BSA, especially at higher nanoparticle concentrations, resulting in lower IC_{50} value under each radiation dose. One underlining mechanism of such enhancement might be ascribed to the catalase-mimic of BiMn/BSA for oxygenation, which provides O_2 substrate of radiotherapy. The DNA radicals produced by radiation would react with such *in-situ* generated oxygen to form irreparable DNA damages (*i.e.*, DNA double strand breaks), thus causing cell death [36].

To confirm the above results, green fluorescent 2′,7′-dichlorodihydrofluorescein diacetate (DCFH-DA) kit was employed to probe intracellular ROS production. Compared to the control, the cells with nanoparticles treatment only emitted weak fluorescence, while the signal became significantly intensified upon radiation, demonstrating the radiotherapy-induced ROS production (Fig. 2E). The fluorescence was further quantified by flow cytometry, and the nanoparticles showed obviously higher intensity than RT alone, confirming the radiosensitization effect of the Bi-containing nanoparticles (Fig. 2F and Fig. S4 in Supporting information). Moreover, the intensity of BiMn/BSA group was 1.7-fold stronger than Bi/BSA, further demonstrating the benefit of Mn incorporation. The over-production of ROS could break DNA to induce cell death, and this can be probed by DNA damage assay kit of γ-H2AX immunofluorescence. The γ-H2AX fluorescence was clearly seen inside cells upon RT, and notably, the signal was highly colocalized with the 4′,6-diamidino-2-phenylindole (DAPI) fluorescence, indicating that the damage mainly occurred in cell nuclei (Fig. 2G and Fig. S5 in Supporting information). Consistent with the above results, Bi-containing nanoparticles showed strong radiosensitization effect, and BiMn/BSA achieved better efficacy.

Besides self-oxygenation, Mn-based nanoparticles were also known to activate STING pathway *via* the release of Mn^{2+}. Mn^{2+} can bind to cyclic GMP-AMP synthase (cGAS) by elevating both the enzymatic activity of cGAS and the dsDNA sensitivity, thereby boosting the activity of STING through the enhanced cGAMP-STING binding affinity [20]. Meanwhile, the activation of STING pathway could maintain ROS homeostasis, showing the potential to sensitize ROS-based RT [37]. To explore the activation of STING by BiMn/BSA, we analyzed the expression of p-STING and STING by Western blotting. Among the treatments, only BiMn/BSA groups displayed the enhancement of STING phosphorylation (Figs. 2H and I, Fig. S6 in Supporting information), indicating STING pathway activation. Therefore, the advantages of BiMn/BSA with Mn incorporation can be summarized into two aspects: its catalase-mimic activity and the release Mn^{2+} to activate STING pathway, which promote ROS generation and DNA damage. As a result, a significantly enhanced RT was achieved to induce tumor cells cycle arrest, senescence and apoptosis.

To further explore the cell death pathway, the cells were dual-stained with Annexin V-fluorescein isothiocyanate (FITC) and ethidium bromide propidium iodide (PI), based on which the detailed information of cell death can be obtained. The amount of

late apoptotic cells significantly increased after RT, and such effect was further pronounced when combining Bi/BSA or BiMn/BSA nanoparticles (Fig. 2J and Fig. S7 in Supporting information). Again, the best efficacy was seen in RT plus BiMn/BSA group, causing >90% cells apoptosis (Fig. 2K and Fig. S8 in Supporting information). Collectively, all these results demonstrated the superiority of BiMn/BSA as nanoradiosensitizer owing to the incorporation of Bi and Mn elements.

The above results demonstrated the radiosensitization and self-oxygenation activities of BiMn/BSA, which is highly suitable to treat the inner hypoxia tumor. However, while EPR effect could facilitate nanoparticles to reach peripheral tumor region, their deep penetration into inner region is usually hindered by the dense ECM. Therefore, the regulation of tumor microenvironment to promote the intratumoral distribution of BiMn/BSA is the prerequisite for its anti-tumor efficacy. Interestingly, previous studies have indicated the multiple regulation effects of RT on tumor microenvironment. For example, RT could induce tumor cells secretion of mononuclear macrophage chemoattractant proteins (MCPs), chemoattractant factors and cytokines, as well as the release of ATP and high mobility group box 1 (HMGB1), resulting in significant recruitment of macrophages into tumor [38,39]. The accumulation of macrophages then upregulates metalloproteinases levels such as MMP-2 and MMP-9, which degrade ECM. Given such ECM-regulation activity, we suspected that RT might be a potential strategy to break the natural barrier of ECM for nanoparticles penetration into tumor, and several experiments were performed.

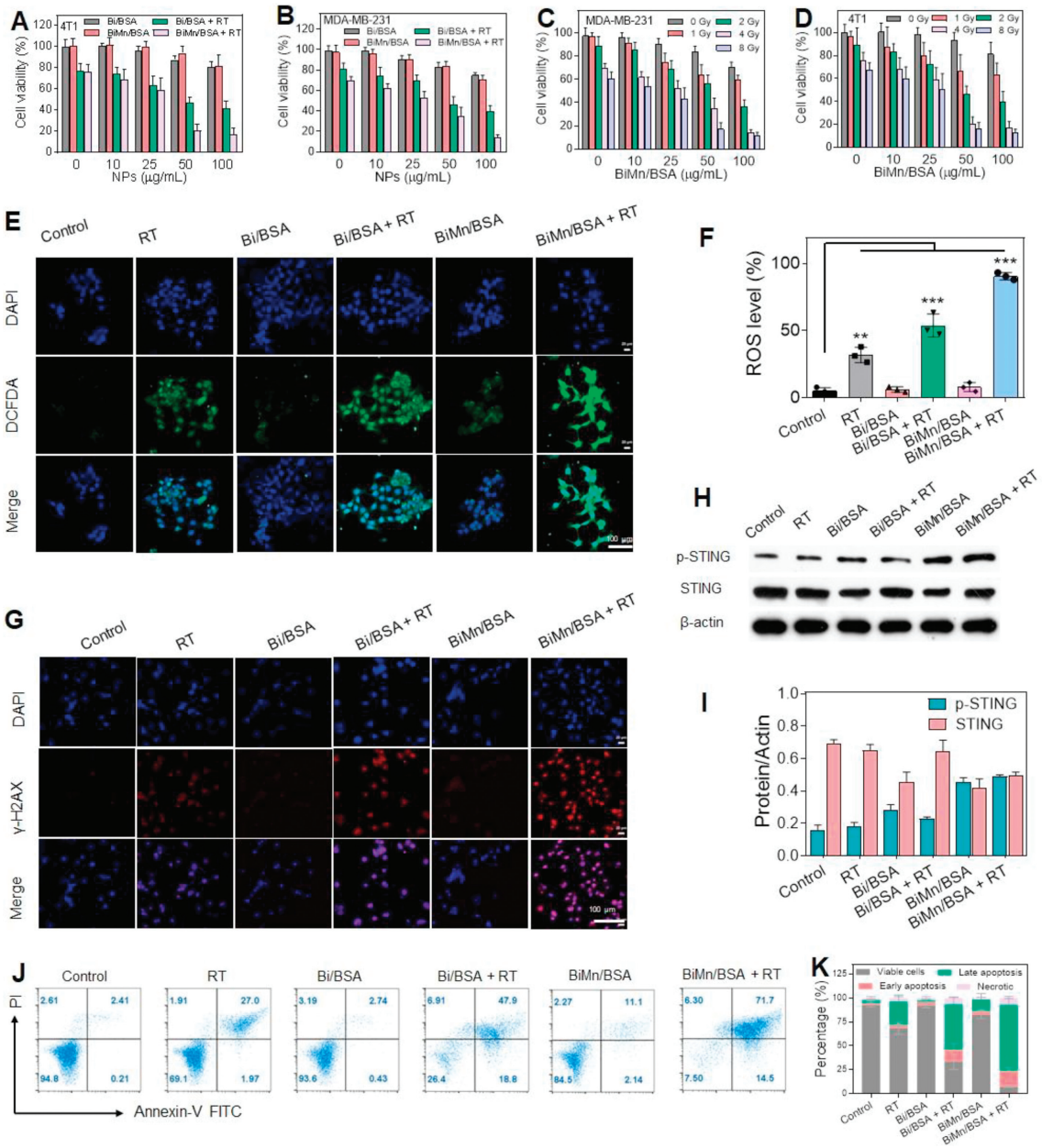

Fig. 2. The viability of (A) 4T1 cells and (B) MDA-MB-231 cells after different treatments. The viability of (C) 4T1 cells and (D) MDA-MB-231 cells exposed to different doses of X-ray radiation with different concentrations of BiMn/BSA ($n = 5$). (E) Confocal fluorescence images probing the ROS. Scale bar: 100 μm. (F) Flow cytometry analysis the intracellular ROS levels in 4T1 cells after various treatments. (G) Confocal fluorescence images of γ-H2AX after various treatments. Scale bar: 100 μm. (H) The expression levels of STING and p-STING proteins evaluated by Western blot and (I) quantified analysis after various treatments. (J) Flow cytometry analysis of the death of 4T1 cells with different treatments and (K) corresponding rate of viable, early apoptosis, late apoptosis and necrotic cells ($n = 3$). Quantitative results are presented as mean ± SD. Differences among multiple groups were assessed using one-way ANOVA. $^{**}P < 0.01$, $^{***}P < 0.001$.

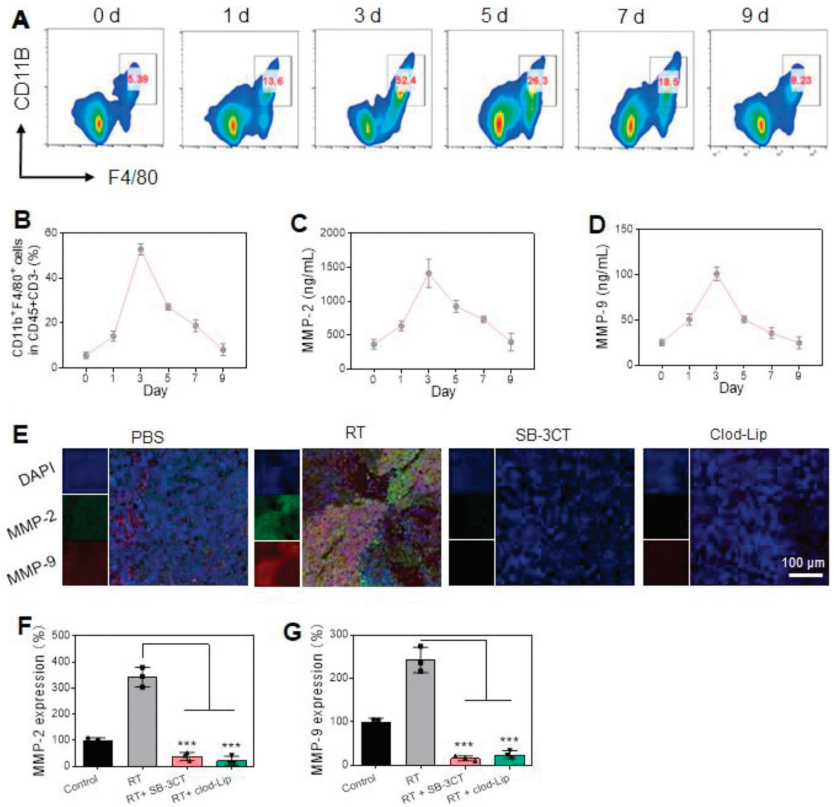

Fig. 3. (A) Flow cytometry to determine the abundance of F4/80$^+$CD11b$^+$ TAMs in 4T1 tumors at various timepoints following 4 Gy RT treatment, and (B) the quantification of macrophages in the tumor microenvironment. ELISA analysis the levels of (C) MMP-2 and (D) MMP-9 in corresponding tumor tissues. (E) Immunofluorescence staining showing the MMP-2 and MMP-9 in tumors with different treatments. Quantitative analysis of Western blot detection for (F) MMP-2 and (G) MMP-9 in tumor tissues with different treatments. Quantitative results are presented as mean ± SD ($n = 3$). Differences among multiple groups were assessed using one-way ANOVA. $^{***}P < 0.001$.

Considering the safety, a low dose RT (4 Gy) was performed on tumor-bearing mice, and the tumor microenvironment was dynamically monitored. Tumor-related macrophages (F4/80$^+$CD11b$^+$) were measured by flow cytometry. As expected, macrophages immediately increased after radiation therapy, and peaked on day 3, followed by a leveling-off (Figs. 3A and B). On day 9 after radiation, the macrophages level reduced to baseline. Therefore, RT induced a dynamic macrophages infiltration. In line with this, the level of MMP-2 and MMP-9 were measured by an enzyme-linked immunosorbent assay (ELISA) kit, which also showed a dynamic fluctuation (Figs. 3C and D). Consistently, these metalloproteinases peaked on day 3, and returned to normal level on day 9. To allow direct observation, MMP-2 and MMP-2 in tumor region was stained with green and red fluorescence, respectively. Both green and red signals were significantly intensified on day 3 after RT (Figs. 3E–G). Such enhancement can be blocked by SB-3CT, a thiol-based inhibitor that can inhibit the expression of MMP-2 and MMP-9. Importantly, the clodronate liposomes (Clod-Lip), a macrophage exhauster, could also abolish the upregulation of MMP-2/MMP-9 level, demonstrating the critical role of macrophages on the upregulation of these proteins. Overall, low dose of RT could temporally modulate tumor ECM *via* macrophages infiltration and MMP-2/MMP-9 expression, which opens a window period to allow deep penetration of the nanoparticles.

Having confirmed the ECM-regulation effect of RT, we next aimed to employ such mechanism to deliver nanoparticles. As indicated by the above results, nanoparticles with Cy5.5 labeling were administrated on day 3 post-RT. Upon vein injection, the fluorescence was eventually seen throughout the mice body in 1 h, indicating broad biodistribution of the nanoparticles. The nanoparticles were gradually eliminated with decreased fluorescence, while selective accumulation into tumor was seen at 12 h and 24 h, owing the EPR effect (Fig. 4A). Notably, it seems that mice with RT showed an obviously stronger fluorescence at tumor than that of non-RT group. To confirm this, major organs and tumor tissues were extracted at 24 h for *ex vivo* imaging, and we indeed observed a much brighter signal for RT + BiMn/BSA group (Fig. 4B). For more accurate quantification, Bi and Mn level was measured by inductively coupled plasma (ICP), which was 6.1-fold and 5.4-fold higher for RT group (Figs. 4C and D). Therefore, more BiMn/BSA were delivered into tumor when combining with a low-dose RT. Actually, such effect has been demonstrated in our previous work, which was also attributed to RT-induced macrophages infiltration [28]. The tumor infiltrated macrophages not only serve as nanoparticles drug depots, but also elicit bursts of extravasation to enhance drug uptake into tumor, both of which could enhance drug uptake into tumor. It is essential to note that all animal experiments in this study were conducted in strict adherence to ethical guidelines for animal use and care at Central South University. Approval for these experiments was granted by the local Institutional Ethics Review Committee.

Given the enhancement of tumor accumulation, we next explored the deep penetration of the nanoparticles with the aid of RT. To do this, tumor tissue was stained by immunofluorescence. Without RT, the Cy5.5 fluorescence from BiMn/BSA was mainly located at the peripheral region of the tumor (Fig. 4E). With RT, on the other hand, the overall fluorescence was much stronger. More importantly, the fluorescence was eventually distributed at both peripheral and inner core regions of tumor, indicating the effective deep penetration of the nanoparticles. BiMn/BSA was further monitored by MRI imaging since Mn as a contrast agent can enhance scan signal generation and reduce signal relaxation time

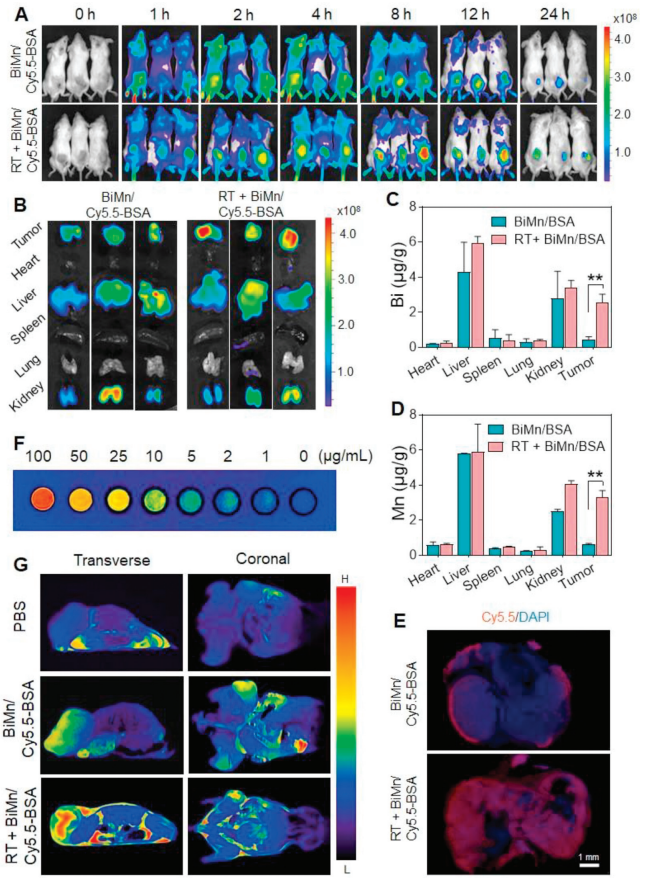

Fig. 4. (A) *In vivo* images showing the dynamic biodistribution of BiMn/Cy 5.5-BSA post nanoparticles injection and (B) *ex vivo* imaging of fluorescence in tumors and main organs at 24 h post administration. (C) Bi and (D) Mn contents in main organs and tumors at 24 h post-injection of BiMn/Cy 5.5-BSA measured by ICP-MS. (E) Penetration and distribution of BiMn/BSA into tumor at 24 h post injection. Scale bar: 1 mm. (F) T1-weighted contrast-enhanced MRI images of different concentrations of BiMn/BSA into PCR tubes. (G) Mouse tumor MRI T1 images of tumors after different treatment. Quantitative results are presented as mean ± SD ($n = 3$). Differences among multiple groups were assessed using one-way ANOVA. $^{**}P < 0.01$.

(Fig. 4F). Concordant with the above results, BiMn/BSA plus RT showed significantly stronger MRI signal, especially at central core region (Fig. 4G). Therefore, a single low-dose RT provides dual-benefits for tumor targeting delivery of the nanoparticles, which not only promotes the accumulation of nanoparticles into tumor, but also facilitates their deep penetration into central tumor core.

Effective tumor accumulation and deep penetration were critically important for the efficacy of nanomedicines. To confirm these benefits, the *in vivo* anti-tumor efficacy of BiMn/BSA-sensitized RT was explored. The mice were randomly divided into six groups, each receiving one of the following treatments as illustrated in Fig. 5A, G1: PBS control, G2: RT, G3: Bi/BSA, G4: RT + Bi/BSA, G5: BiMn/BSA, and G6: RT + BiMn/BSA. Two doses of 4 Gy radiation were performed on day 0 (for tumor targeting delivery and deep penetration of the nanoparticles) and day 4 (for RT), respectively. Tumor volume was recorded every other day to evaluate the therapeutic effect. Compared to the PBS control, RT alone did not show much anti-tumor effect due to the low radiation dose with limited energy, and the nanoparticles did not have a significant impact on tumor proliferation either (Fig. 5B). When RT combined with nanoparticles, by contrast, significant tumor inhibitions were observed, attributable to the radiosensitization effect of the Bi element. In addition, radiation-induced accumulation and deep penetration of nanoparticles might also contribute to the enhanced anti-tumor effect. Among then, RT + BiMn/BSA group displayed the best therapeutic outcome, which could completely suppress the tumor growth. The mice were sacrificed after therapies to collect the tumor tissues, and the tumor suppression effect can be directly compared with an order of RT + BiMn/BSA > RT + Bi/BSA > BiMn/BSA > RT > Bi/BSA > PBS (Fig. 5C).

To have mechanistic understanding, the tumor tissues were further examined *via* pathological analyses. The strongest signal of immunofluorescence from both green fluorescent Tunnel protein and red fluorescent caspase 3 was observed for RT + BiMn/BSA group, demonstrating the best efficacy to induce tumor cell apoptosis (Fig. 5D and Fig. S9 in Supporting information). Hematoxylin and eosin (H&E) staining was also performed and the same trend was observed. Moreover, the expression of γ-H2AX in the tumor tissues significantly increased, demonstrating RT-induced DNA damage. Notably, all these pathological analyses further evidenced the superiority of BiMn/BSA over Bi/BSA to combat tumor. These can be ascribed to two aspects. First, Mn-incorporation could endow the nanoparticles with catalase-mimic activity, which served as self-oxygenator to support O_2. This can be evidenced by the hypoxia-inducible factor 1-alpha (HIF-1α) immunofluorescence, which became significantly weakened for RT + BiMn/BSA group. Second, the release of Mn^{2+} from BiMn/BSA could activate STING pathway, which in turn sensitizes the RT by preventing DNA damage repair. To verify this, the level of STING and p-STING proteins were measured by western blotting, and their relative ratio was quantified. Obviously, the STING protein decreased accompanied by p-STING protein decrease after BiMn/BSA therapies, suggesting the activation of STING pathway to induce protein phosphorylation (Figs. 5E and F, Fig. S10 in Supporting information). Collectively, BiMn/BSA presents as a multi-functional nanoradiosensitizer for enhanced RT by virtue of high-*Z* characteristic of bismuth, catalase-mimic activity of the nanoparticles, as well as the release of Mn^{2+} to activate STING pathway.

Another important limitation of traditional RT is the non-specific damage to nearby normal tissues. In our system, low-dose radiation was performed and biocompatible nanoradiosensitizer was employed, which was expected to decrease side-effects for better clinical application. To confirm this, the biosafety was systematically evaluated. The body weights of mice did not show significant change during therapies, indicating the lack of acute toxicity (Fig. 5G). Key serum biochemistry parameters were tested, and all of them were within the normal change, suggesting the minimal influence on liver/kidney functions and cardiac enzyme profile (Fig. S11 in Supporting information). Hematological analysis indicated that there were no significant changes in red blood cell, white blood cell, or platelet counts after therapies (Fig. S12 in Supporting information). Moreover, the H&E staining of various organs revealed no apparent inflammation or damage (Fig. S13 in Supporting information). Therefore, this combinatorial strategy could mitigate the intrinsic limitation of RT with lower side-effects, which would definitely be more compliant to tumor patients.

In conclusion, we have developed BiMn/BSA nanoparticles as a novel nanoradiosensitizer with multiple mechanisms to enhance radiotherapy efficacy. By incorporating Bi/Mn through biomineralization, these nanoparticles exhibit excellent radiosensitizing properties. Furthermore, we have discovered a previously unexplored phenomenon where low-dose radiotherapy induces the recruitment of macrophages to the tumor site, which significantly improves the accumulation and deep penetration of nanoparticles within the tumor. Our findings highlight the crucial role of macrophages in modulating the tumor microenvironment by upregulating metalloproteinases, thereby promoting the degradation of the extracellular matrix and facilitating the penetration of nanoparticles into the tumor core. *In vivo* studies have demonstrated the remarkable potential of combining low-dose radiotherapy with BiMn/BSA nanoparticles, resulting in enhanced radio-

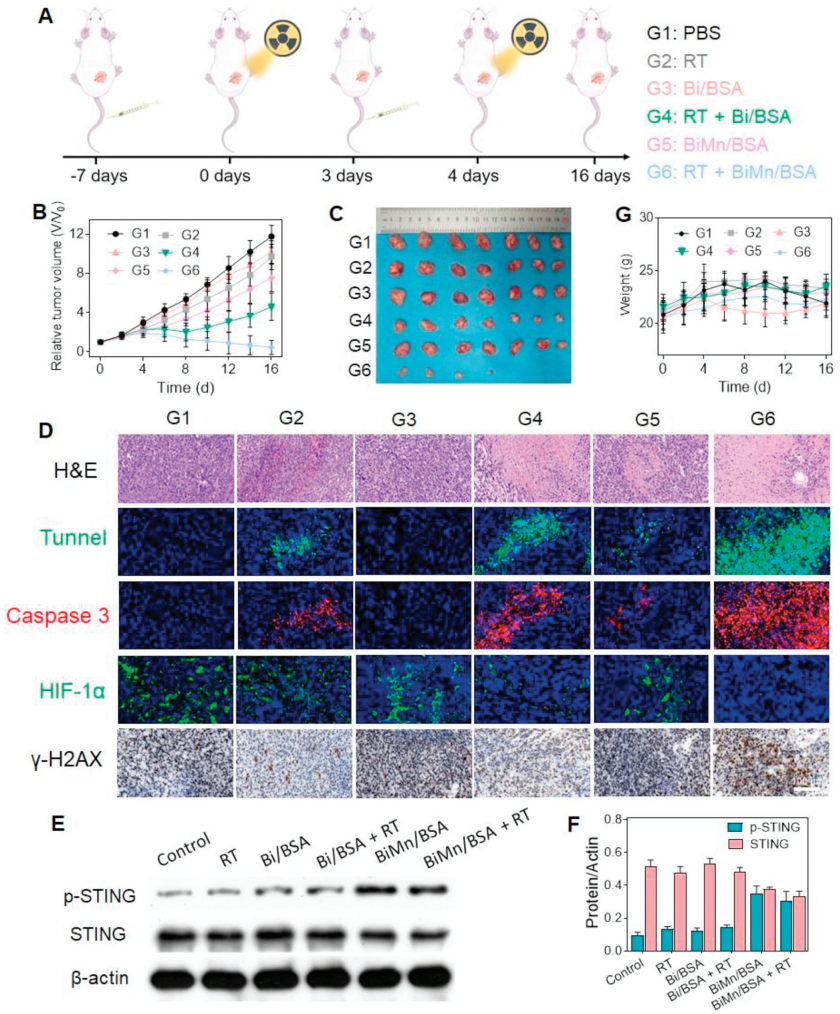

Fig. 5. (A) Overall treatment schedule of *in vivo* anti-tumor experiment ($n = 7$). (B) Changes of tumor volume during various treatments. (C) Photographs of tumors harvested after different treatments. (D) H&E, terminal deoxynucleotidyl transferase dUTP nick end labeling (TUNEL), caspase 3, HIF-1α, and γ-H2AX staining to evaluate necrosis, apoptosis, tumor hypoxia, and nuclear damage of tumor after various treatments. Scale bar: 100 μm. (E) The level of STING and p-STING proteins after treatments, and (F) a quantitative analysis. In each panel, G1, PBS; G2, RT; G3, Bi/BSA; G4, RT + Bi/BSA; G5, BiMn/BSA; G6, RT + BiMn/BSA ($n = 3$). Quantitative results are presented as mean ± SD. Differences among multiple groups were assessed using one-way ANOVA.

therapy efficacy and complete tumor eradication. Importantly, this therapeutic approach maintains full biocompatibility, ensuring its safe application in clinical settings. Our research sheds light on the effectiveness of metal-based nanoradiosensitizers and the significance of macrophage-mediated tumor accumulation in overcoming the limitations of conventional radiotherapy. By leveraging these approaches, we can improve the delivery of therapeutic agents to tumors and enhance their deep penetration into the tumor microenvironment. This study opens new avenues for improving nanoparticle radiotherapy sensitization, holding great promise for enhancing treatment outcomes in cancer patients.

Declaration of competing interest

The authors declare that they have no known competing financial interests or personal relationships that could have appeared to influence the work reported in this paper.

Acknowledgments

This work received support from the following funding sources in descending order of magnitude: the National Natural Science Foundation of China (Nos. 81771827, 82071986, 82372072), the Key Research and Development Program of Hunan Province (No. 2022SK2025), the Natural Science Foundation of Hunan Province (Nos. 2023JJ40966, 2021JJ20084), the Science and Technology Program of Hunan Province (Nos. 2021RC4017, 2021RC3020), the Youth Science Foundation of Xiangya Hospital (No. 2022Q13), the Central South University Frontier Cross-disciplinary Project (No. 2023QYJC021), the China Postdoctoral Science Foundation (No. 2023M733954) and the National Postdoctoral Program for Innovative Talents (No. BX20230432).

Supplementary materials

Supplementary material associated with this article can be found, in the online version, at doi:10.1016/j.cclet.2024.109632.

References

[1] K. Wang, J.E. Tepper, CA Cancer J. Clin. 71 (2021) 437–454.
[2] D.C. Singleton, A. Macann, W.R. Wilson, Nat. Rev. Clin. Oncol. 18 (2021) 751–772.
[3] X. Yu, H. Ma, G. Xu, Z. Liu, Chin. Chem. Lett. 33 (2022) 4169–4174.
[4] C. Monteiro, L. Miarka, M. Perea-Garcia, et al., Nat. Med. 28 (2022) 752.
[5] F.G. Herrera, M. Irving, L.E. Kandalaft, G. Coukas, Lancet Oncol. 20 (2019) E417–E433.
[6] W.S.M.E. Theelen, H.M.U. Peulen, F. Lalezari, et al., JAMA Oncol. 5 (2019) 1276–1282.

[7] X. Zhou, M. You, F. Wang, et al., Adv. Mater. 33 (2021) 2100556.
[8] X. Guan, L. Sun, Y. Shen, et al., Nat. Commun. 13 (2022) 2834.
[9] H. Huang, C. Zhang, X. Wang, et al., Nano Lett. 20 (2020) 4211–4219.
[10] X. Chen, J. Song, X. Chen, H. Yang, Chem. Soc. Rev. 48 (2019) 3073–3101.
[11] Y. Pan, W. Tang, W. Fan, J. Zhang, X. Chen, Chem. Soc. Rev. 51 (2022) 9759–9830.
[12] P. Pei, T. Liu, W. Shen, Z. Liu, K. Yang, Mater. Horiz. 8 (2021) 1348–1366.
[13] Z. Guo, S. Zhu, Y. Yong, et al., Adv. Mater. 29 (2017) 1704136.
[14] Y. Zang, L. Gong, L. Mei, Z. Gu, Q. Wang, ACS Appl. Mater. Interfaces 11 (2019) 18942–18952.
[15] F. Cai, K. Ye, M. Chen, et al., Chin. Chem. Lett. 34 (2023) 107945.
[16] L. Wu, W. Wu, J. Zhang, et al., Cancer Discov. 12 (2022) 2820–2837.
[17] T. Zhou, X. Liang, P. Wang, et al., ACS Nano 14 (2020) 12679–12696.
[18] M. Lv, M. Chen, R. Zhang, et al., Cell Res. 30 (2020) 966–979.
[19] X. Sun, Y. Zhang, J. Li, et al., Nat. Nanotechnol. 16 (2021) 1260–1270.
[20] C. Wang, Y. Guan, M. Lv, et al., Immunity 48 (2018) 675–687 e7.
[21] C. Li, Y. Zhang, Y. Wan, et al., Chin. Chem. Lett. 32 (2021) 1615–1625.
[22] C. Li, J. Wang, Y. Wang, et al., Acta Pharm. Sin. B 9 (2019) 1145–1162.
[23] L. Kong, C. Yang, Z. Zhang, Adv. Sci. 10 (2023) e2204178.
[24] F. Boateng, W. Ngwa, Int. J. Mol. Sci. 21 (2019) 273.
[25] I. de Lazaro, D.J. Mooney, Nat. Mater. 19 (2020) 486–487.
[26] S. Son, J.H. Kim, X. Wang, et al., Chem. Soc. Rev. 49 (2020) 3244–3261.
[27] Z. Zhou, X. Liu, D. Zhu, et al., Adv. Drug Deliv. Rev. 115 (2017) 115–154.
[28] J. Liu, L. Guo, Z. Mi, et al., J. Control. Release 348 (2022) 1050–1065.
[29] M.A. Miller, R. Chandra, M.F. Cuccarese, et al., Sci. Transl. Med. 9 (2017) eaal0225.
[30] S. Bissinger, C. Hage, V. Wagner, et al., Sci. Transl. Med. 13 (2021) eabd4550.
[31] H. Iqbal, T. Yang, T. Li, et al., J. Control. Release 329 (2021) 997–1022.
[32] X. Yu, W. Zhu, Y. Di, et al., Int. J. Nanomed. 12 (2017) 6771–6785.
[33] P. Liu, Y. Zhou, X. Shi, et al., J. Nanobiotechnol. 19 (2021) 149.
[34] P. Liu, X. Xie, M. Liu, et al., Acta Pharm. Sin. B 11 (2021) 823–834.
[35] Q. Chen, J. Chen, C. Liang, et al., J. Control. Release 263 (2017) 79–89.
[36] J.M. Brown, W.R. William, Nat. Rev. Cancer 4 (2004) 437–447.
[37] T.J. Hayman, M. Baro, T. MacNeil, et al., Nat. Commun. 12 (2021) 2327.
[38] F. He, J. Bai, J. Wang, et al., J. Cell Physiol. 234 (2019) 17314–17325.
[39] D. Ai, Y. Dou, Z. Nan, et al., Front. Oncol. 11 (2021) 740622.